Disentangling elastic and inelastic scattering pathways in the intersubband electron dynamics of *n*-type Ge/SiGe quantum fountains

Luigi Bagolini,[1,*] Michele Montanari,[1,*] Luca Persichetti,[1,†] Luciana Di Gaspare,[1] Giovanni Capellini,[1,2] Michele Ortolani,[3] Monica De Seta,[1] and Michele Virgilio[4]

[1]*Dipartimento di Scienze, Università degli Studi Roma Tre, V.le G. Marconi 446, I-00146 Rome, Italy*
[2]*IHP-Leibniz-Institut für Innovative Mikroelektronik, Im Technologiepark 25, D-15236 Frankfurt (Oder), Germany*
[3]*Dipartimento di Fisica, Università di Roma "Sapienza", Piazzale A. Moro 2, I-00185 Rome, Italy*
[4]*Dipartimento di Fisica "E. Fermi", Università di Pisa, Largo Pontecorvo 3, I-56127 Pisa, Italy*

(Received 13 March 2020; revised manuscript received 4 May 2020; accepted 12 May 2020; published 4 June 2020)

n-type Ge/SiGe quantum wells have been suggested as a promising platform for the realization of a Si-compatible THz laser. Focusing on this material system, we have developed a numerical model to describe the intersubband carrier dynamics which restores the equilibrium after pulsed optical excitation in asymmetric coupled Ge/SiGe quantum wells. We take into account inelastic and elastic scattering processes and investigate different quantum-well geometries, doping densities, and excitation regimes. In this configuration space, we disentangle the effect on the overall dynamics of each scattering channel and provide intersubband relaxation times, finding larger values with respect to III-V based materials, thanks to the weaker electron-phonon coupling with respect to III-V compounds. Finally, the model is used to study and optimize the population inversion between the first- and second-excited subband levels and to assess its dependence on the lattice temperature, providing a sound theoretical framework to guide forthcoming experiments.

DOI: 10.1103/PhysRevB.101.245302

I. INTRODUCTION

Intersubband transitions (ISBTs) in semiconductor quantum wells (QWs) are the key mechanisms behind the operation of many mid-infrared/terahertz optoelectronic devices, such as quantum cascade lasers (QCLs) [1–3], quantum fountains [4–6], and quantum-well infrared photodetectors (QWIPs) [7]. Furthermore, the use of unipolar ISBTs has been proposed as a viable route for the realization of light emitters employing silicon-compatible group-IV materials, such as Ge, Sn, and their alloys [8,9], thus overcoming the intrinsically poor optical emission properties due to the indirect band gap featured by this class of semiconductors. In addition to the possible integration in the complementary metal-oxide-semiconductor (CMOS) platform, the use of SiGe heterostructures for the development of an ISBT-based laser would benefit from the absence of the strong electron-phonon coupling typical of polar lattices. This fact should allow higher-temperature operation in the THz range. As a matter of fact, experiments with GaAs QWs have demonstrated that, above 40 K, the intersubband (ISB) lifetimes are limited by the polar optical phonon scattering mechanism [8,10], while, in similar studies on Si/SiGe and Ge/SiGe heterostructures, no lifetime reduction has been observed up to 100 K [11].

For the realization of a Si-compatible THz light source, *n*-type Ge/SiGe QW structures grown on top of a Si(001) substrate are particularly promising. Indeed, the conduction band offset in this material system is in the order of 120 meV [12], a value large enough to design optical emitters leveraging on ISBTs in the THz range. Moreover, the relatively low (001) confinement mass $m^* = 0.13\ m_0$ associated to Ge *L*-valley electrons, and the expected long ISB relaxation times [11] could provide gain values comparable to those demonstrated in GaAs THz QCLs at low temperatures and, potentially, also allow room-temperature operation [13]. Although one of the main challenges in the realization of SiGe devices is their large lattice mismatch with the Si substrate, the growth of high-quality Ge/SiGe QW heterostructures featuring a large number of module repetitions has been recently made available thanks to the high degree of control achieved in the deposition process [14–16]. The observation of narrow ISBT absorption peaks in the 4-12 THz range [6,17–20] and the very recent measurement of photoluminescence emission in the THz range [21], confirm that *n*-type Ge/SiGe QWs are excellent candidates for the realization of a silicon-compatible THz emitter.

A further step toward this goal has been recently reported in Ref. [14] where the ISBT features of *n*-type asymmetric coupled quantum wells (ACQW) have been studied, demonstrating a high degree of control on the electronic spectrum and on the spatial properties of the relevant wave functions. Remarkably, asymmetric QWs can be regarded as a very interesting playground system since they represent the basic building block of more complex cascade architectures. At the same time, being three-level systems, asymmetric QWs are useful to study the population inversion under optical excitation

*These authors contributed equally to this work.
†luca.persichetti@uniroma3.it

 ©2020 American Physical Society

(the so-called quantum fountain scheme), circumventing, in this way, the difficulties related to the fabrication of electrical contacts needed to efficiently sustain the vertical transport of carriers in a QCL device. Finally, asymmetric QWs also represent the simplest model structure to gain insights into the ISB carrier dynamics driving back the system to the equilibrium after an excitation. To this end, the development of a reliable modeling platform is highly desirable, both to interpret time-resolved optical experiments, which probe the carrier relaxation dynamics [22], and to optimize the quantum structure, targeting the most suitable subband lifetimes to achieve population inversion. In order to have an effective predictive capability, such platform must include a dynamic tracking of the out-of-equilibrium populations and the carrier energy distribution in all the relevant subbands. Even if, in many situations, the ISB relaxation dynamics is dominated by the electron-phonon coupling [23], an accurate dynamic model must also take into account other interactions, such as ionized impurity, electron-electron, and interface roughness scatterings [24,25]. Finally, the model should also include carrier heating effects since, when the ISB energy spacing is below the phonon energy, the optical phonon (OP) emission can be thermally activated [10], greatly affecting the relaxation rates. As a matter of fact, such a complete modeling platform, targeting group-IV based materials, was not hitherto developed. From a more general perspective, such model would significantly improve our understanding of the ISB relaxation dynamics occurring in the presence of nonpolar lattice excitations, also clarifying whether elastic scattering channels substantially contribute to limiting the subband lifetimes, up to noncryogenic temperatures. Furthermore, a numerical model for group-IV based multilayer systems could be calibrated against a suitable set of time-resolved experimental data, thus enabling a precise evaluation of the parameters governing each scattering channel in the SiGe material system, filling, in this way, another relevant knowledge gap. To better appreciate this point, we notice that, to take into account the electron-phonon interaction in the modeling of ISB unipolar optoelectronic devices, authors usually rely on values of the deformation potentials which have been never directly measured [26]. Moreover, these literature parameters refer to the electron-phonon coupling in bulk systems, despite it is not clear *a priori* if the same values are still suitable to describe the interaction in low-dimensional multilayer structures [9].

In this paper we introduce and discuss a rate equation model, which addresses the ISB dynamics in three-level SiGe multilayer systems, and relies on a set of differential equations describing, in the framework of the first-order perturbation theory, the energy and particle fluxes among the different subbands. Subsequently, we use the model to produce numerical data which shed light on the ISB relaxation dynamics occurring in *n*-type asymmetric Ge/SiGe quantum-well structures after a pulsed optical pumping, set to be resonant with the transition between the fundamental and the second-excited levels. Two families of asymmetric quantum-well geometries are considered, featuring different subband energy separations, wave-function overlap, number of heterointerfaces, and doping concentrations. The effect of design parameters and lattice temperature on the population inversion between the second- and first-excited subband levels is also discussed.

II. MODEL DESCRIPTION

In this section, we describe the theoretical framework adopted to study the ISB electron dynamics in optically excited strain-compensated *n*-type Ge-rich Ge/SiGe quantum-well structures. Focus is given on the ISB relaxation dynamics which occurs after optical excitation via a pulsed laser beam driven at a frequency resonant with the ISB energy spacing between the second-excited and the fundamental subband. The investigated systems are (001) ACQWs, designed to engineer the energy position and wave functions of the first three subbands states associated to the fourfould-degenerate L valleys. We first calculate the equilibrium electronic states at a given lattice temperature T^L by means of a multivalley effective mass Schrödinger-Poisson solver, taking into account the strain in the individual layers and the contributions to the Hartree potential from electrons at the Γ, Δ, and L valleys, and including exchange-correlation effects in the local density approximation [14,27]. We remark that the validity of effective mass description is well established in predicting intersubband and interband optoelectronic properties of semiconductor heterostructures having layer thickness in the order of few nanometers, as in this work [18,27,28].

For each subband i, with $i = 1, 2, 3$, we evaluate the subband bottom energy E_i^0, the envelope wave function $\psi_i(z)$, and the two-dimensional (2D) equilibrium carrier densities N_i, as resulting from the complete ionization of phosphorus donor atoms located in the Ge well material [11,29]. When the system is optically excited via resonant pumping of the $1 \rightarrow 3$ transition, the carriers are driven out of equilibrium and start to exchange energy with both the photon and phonon fields through ISB and intrasubband scattering events, involving initial and final states which can belong to the same (intravalley) or to different (intervalley) degenerate L valleys. Since in the analyzed Ge/SiGe heterostructures Δ_2 states are confined in a different spatial region with respect to the L states [see Figs. 1(a) and 1(b)], scattering events involving those states are expected to play a negligible role due to the small wave-function overlap, similarly to what is reported in Refs. [22,30].

To numerically describe the ISB dynamics at the picosecond scale, we assume that the time-dependent electron populations in each subband are, at each time step, instantaneously and independently thermalized due to the presence of fast elastic intrasubband scattering processes, as suggested by Monte Carlo simulations [31]. Under this hypothesis, three time-dependent Fermi distributions are introduced to describe the energy dispersion of the carriers. Each of them is characterized by a time-dependent electronic temperature $T_i^e(t)$ and chemical potential $\mu_i(t)$, with $i = 1, \dots, 3$. These quantities are evaluated as a function of the total subband energy $E_i(t)$ per unit of surface, associated to the presence of the 2D carrier density N_i, solving

$$N_i(t) = D \int_{E_i^0}^{\infty} \frac{dE}{1 + e^{(E-\mu_i)/k_B T_i^e}}, \quad (1)$$

$$E_i(t) = D \int_{E_i^0}^{\infty} \frac{E\, dE}{1 + e^{(E-\mu_i)/k_B T_i^e}}, \quad (2)$$

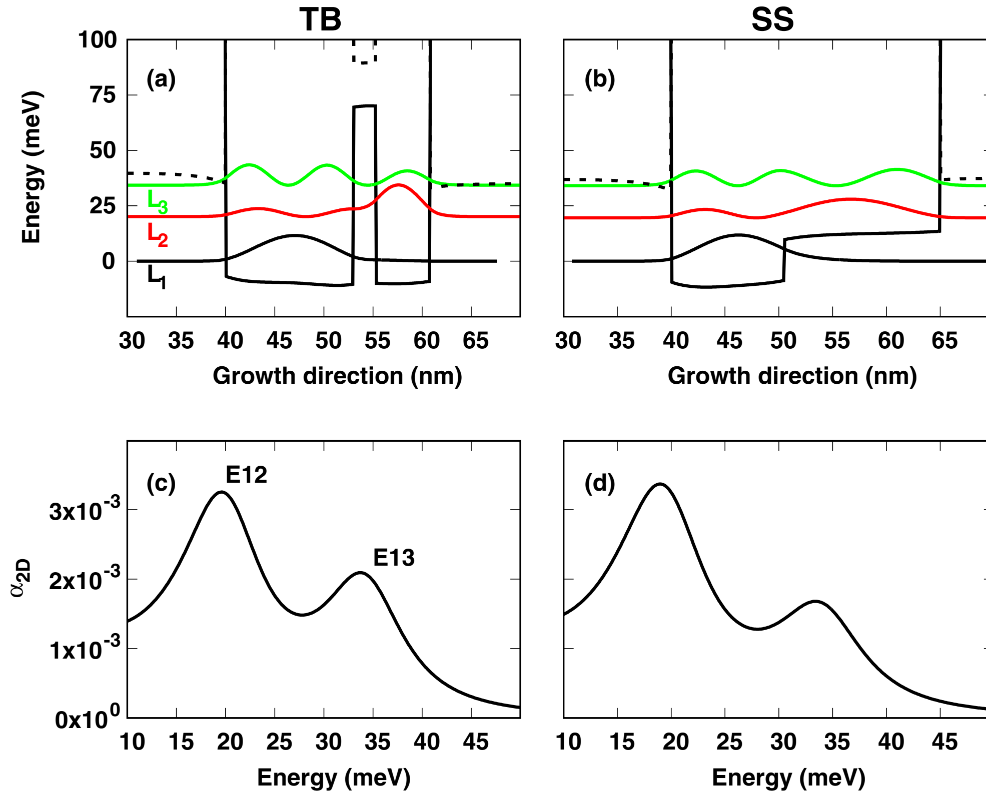

FIG. 1. Electron energy and squared wave function for (a) the tunneling barrier system (TB) and (b) the stepwise structure (SS). Solid and dashed black curves represent the L and Δ_2 band profiles, respectively. The electron population in the first confined state is $n_{2D} = 5 \times 10^{11}$ cm^{-2} for both the systems. The two systems have been optimized in order to obtain similar absorption spectra at $T^L = 4$ K, shown in in (c) and (d).

where $D = 4m_d/(\pi\hbar^2)$ is the density of states (DOS) (with the inclusion of spin degeneracy) associated to the fourfould-degenerate L valleys of Ge. The DOS mass m_d is the Ge in-plane conduction effective mass, calculated, following Ref. [32], as $m_d = (m_1 m_2)^{1/2}$ with $m_1 = m_t$ and $m_2 = (m_t + 2m_l)/3$. The adopted values for the longitudinal m_l and transverse m_t effective mass are reported in Table I, together with other relevant material parameters used in our model. In the following, we adopt the notation $E_{ji} = E_j - E_i$ for defining the energy associated to the transition between levels i and j.

The dynamical evolution of subband population N_i and energy E_i are obtained starting from their equilibrium value at $t = -\infty$, calculating at each discrete time step their variation caused by intersubband and intrasubband scattering events, according to

$$\begin{aligned}\frac{\partial}{\partial t}N_i = {}& \delta_{i,1}\big(W^{\rm pump}_{3\to1} - W^{\rm pump}_{1\to3}\big) + \delta_{i,3}\big(W^{\rm pump}_{1\to3} - W^{\rm pump}_{3\to1}\big)\\ &+ \sum_{j\neq i}\sum_{intra,inter}\big(W^{\rm OP-}_{j\to i} - W^{\rm OP-}_{i\to j}\big) + \sum_{j\neq i}\sum_{intra,inter}\big(W^{\rm OP+}_{j\to i} - W^{\rm OP+}_{i\to j}\big)\\ &+ \sum_{j\neq i}\big[\big(W^{\rm IFR}_{j\to i} - W^{\rm IFR}_{i\to j}\big) + \big(W^{\rm II}_{j\to i} - W^{\rm II}_{i\to j}\big) + \big(W^{\rm ee}_{j\to i} - W^{\rm ee}_{i\to j}\big)\big], \qquad i, j = 1, 2, 3 \end{aligned} \tag{3}$$

$$\begin{aligned}\frac{\partial}{\partial t}E_i = {}& \delta_{i,1}\big(\overline{W}^{\rm pump}_{3\to1} - \hbar\omega_p W^{\rm pump}_{3\to1} - \overline{W}^{\rm pump}_{1\to3}\big) + \delta_{i,3}\big(\overline{W}^{\rm pump}_{1\to3} + \hbar\omega_p W^{\rm pump}_{1\to3} - \overline{W}^{\rm pump}_{3\to1}\big)\\ &+ \sum_{j\neq i}\sum_{intra,inter}\big[\big(\overline{W}^{\rm OP-}_{j\to i} + \hbar\omega_{\rm eff}W^{\rm OP-}_{j\to i} - \overline{W}^{\rm OP-}_{i\to j}\big) + \big(\overline{W}^{\rm OP+}_{j\to i} - \hbar\omega_{\rm eff}W^{\rm OP+}_{j\to i} - \overline{W}^{\rm OP+}_{i\to j}\big)\big]\\ &+ \sum_{intra,inter}\hbar\omega_{\rm eff}\big(W^{\rm OP-}_{i\to i} - W^{\rm OP+}_{i\to i}\big) - \overline{W}^{\rm AC}_{i\to i}\\ &+ \sum_{j\neq i}\big[\big(\overline{W}^{\rm IFR}_{j\to i} - \overline{W}^{\rm IFR}_{i\to j}\big) + \big(\overline{W}^{\rm II}_{j\to i} - \overline{W}^{\rm II}_{i\to j}\big) + \big(\overline{W}^{\rm ee}_{j\to i} - \overline{W}^{\rm ee}_{i\to j}\big)\big], \qquad i, j = 1, 2, 3. \end{aligned} \tag{4}$$

TABLE I. Literature values for the material parameters adopted in our model. m_l (m_t) is the longitudinal (transverse) effective mass. $\hbar\omega_{\text{eff}}^{\text{intra}}$ ($\hbar\omega_{\text{eff}}^{\text{inter}}$) is the phonon energy of the intravalley (intervalley) optical phonon branch, to which the deformation potential $\Xi_{\text{OP}}^{\text{intra}}$ ($\Xi_{\text{OP}}^{\text{inter}}$) is associated. Δ is the root-mean-square interface roughness amplitude and Λ the interface roughness correlation length, obtained experimentally for the material system.

Parameter	Value
m_l	1.59 ([49]) (m_0)
m_t	0.093 ([49]) (m_0)
$\hbar\omega_{\text{eff}}^{\text{intra}}$	37.07 ([26]) (meV)
$\hbar\omega_{\text{eff}}^{\text{inter}}$	27.56 ([26]) (meV)
$\Xi_{\text{OP}}^{\text{intra}}$	5.5 ([26]) (10^8 eV/cm)
$\Xi_{\text{OP}}^{\text{inter}}$	3.0 ([26]) (10^8 eV/cm)
Δ	2 ([15]) (Å)
Λ	70 ([15]) (Å)

In the above equations, $W_{i\to j}$ ($\overline{W}_{i\to j}$) represents the particle (energy) flux per unit of surface and time from the initial subband i to the final subband j, due to scattering events associated to the perturbative potential specified in the superscript. In particular, we have included in our model, as elastic scattering channels, the interface roughness (IFR), the Coulomb field produced by ionized impurities (II), and the electron-electron interaction (ee), as detailed in the Appendix. The inelastic processes considered are the electron-photon interaction due to the pump beam (pump) and the coupling of carriers with the OP and acoustic (AC) phonon branches. Accordingly, in Eq. (4), $\hbar\omega_p$ represents the pump photon energy, while $\hbar\omega_{\text{eff}}$ indicates the optical phonon energy. The superscripts OP− and OP+ refer to the OP absorption and emission processes, respectively. As for the electron-optical phonon interaction, we also notice that, although not explicitly indicated by the notation adopted in Eq. (4), we use different values for the deformation potential and phonon energy associated to intravalley and intervalley transitions [26] since small and large momentum lattice excitations are involved in the former and latter case, respectively (see Table I). We also stress that different L valleys can be only coupled by zone-edge phonons since all the other scattering rates are fast decreasing functions of the exchanged momentum,. Finally, we notice that, in our model, a subband can relax its energy not only by means of a transfer of carriers to a different subband, but also via intrasubband inelastic processes involving both AC and OPs, as apparent from the presence of the diagonal terms $\overline{W}_{ii}$ in Eq. (4). The rates $W_{i\to j}$ and $\overline{W}_{i\to j}$ are calculated summing over all the available initial and final states in subbands i and j and taking into account the associated carrier population. This summation can be expressed in terms of the energy in the initial state as

$$W_{i\to j} = D\int_{E_{\min}}^{\infty} \frac{dE_i\, W_{i\to j}(E_i)}{1+e^{(E_i-\mu_i)/k_BT_i^e}}\left(1-\frac{1}{1+e^{(E_j-\mu_j)/k_BT_j^e}}\right), \quad (5)$$

$$\overline{W}_{i\to j} = D\int_{E_{\min}}^{\infty} \frac{dE_i\, E_j\, W_{i\to j}(E_i)}{1+e^{(E_i-\mu_i)/k_BT_i^e}}\left(1-\frac{1}{1+e^{(E_j-\mu_j)/k_BT_j^e}}\right), \quad (6)$$

where $E_j = E_i$ for elastic processes or $E_j = E_i \pm \hbar\omega$ when a photon or a phonon is absorbed/emitted; in the above equation $W_{i\to j}(E_i)$ represents the scattering rate for a particle in subband i with initial energy E_i, summed over all the final states in subband j which fulfill the energy conservation constraint. From the energy conservation condition, it also follows that, in the case of elastic scattering $E_{\min} = \max(E_i^0, E_j^0)$, while for inelastic processes $E_{\min} = \max(E_i^0, E_j^0 \mp \hbar\omega_{\text{eff}})$, with the upper and lower signs referring to absorption and emission, respectively. In the Appendix, we will separately discuss in more detail each scattering channel implemented in the model.

III. RESULTS AND DISCUSSION

We apply the model to describe the ISB relaxation dynamics after pulsed optical excitation in two different ACQW structures, which represent common design configurations for realizing a three-level system: the tunneling barrier (TB) and the stepwise geometry (SS) [Figs. 1(a) and 1(b)]. The asymmetry of these structures enables ISB optically coupling among all the three levels L_1, L_2, and L_3, while in symmetric quantum wells optical transitions can occur only between L_1 and L_2, or L_2 and L_3. Allowing for resonant pumping of the L_1-L_3 transition, these geometries have been studied in the literature, targeting population inversion between the L_2 and L_3 levels. In the present case, such asymmetry is realized in the TB design by coupling, through a 2.3-nm-thick $\text{Si}_{0.15}\text{Ge}_{0.85}$ tunnel barrier, a wide Ge well of width $w_L = 13.0$ nm with a thinner one of width $w_T = 5.5$ nm [Fig. 1(a)]; these three layers are sandwiched between 20-nm-thick $\text{Si}_{0.19}\text{Ge}_{0.81}$ spacers. The SS configuration [Fig. 1(b)] features a Ge well of width $w_L = 10.5$ nm and a $\text{Si}_{0.03}\text{Ge}_{0.97}$ step of width $w_S = 14.5$ nm, sandwiched between two 20-nm-thick $\text{Si}_{0.19}\text{Ge}_{0.81}$ spacer layers, as for the TB system. The in-plane lattice parameter was fixed to that of a cubic $\text{Si}_{0.10}\text{Ge}_{0.90}$ alloy. In Fig. 1, the $n_{2\text{D}}$ equilibrium carrier density is equal to 5×10^{11} cm^{-2}, for both the TB and SS configurations. This concentration results from the complete ionization of P impurities in the wide well region for the TB configuration and in the Ge layer for the SS system with a uniform concentration of 3.25×10^{17} cm^{-3} and 4.20×10^{17} cm^{-3}, respectively. To simulate the upward diffusion of P donor atoms occurring during the deposition, we added, to this square doping concentration profile, an exponentially decaying tail in the growth direction, with a characteristic decay length of 20 nm/decade [16].

In the TB system, the wave functions of L_2 and L_3 result from the hybridization of the first-excited state of the large well with the fundamental of the thin well [14]. By a proper choice of the geometrical parameters, the L_1, L_3 wave functions and their energy spacing in the SS systems have been designed to be similar to those of the TB one [compare Figs. 1(a) and 1(b)]. Moreover, the $1\to2$ and $1\to3$ oscillator strengths have been targeted to have comparable values in both the SS and the TB systems. Consequently, the $\alpha_{2\text{D}}$ absorption spectra of SS and TB, featuring equal 2D carrier density $n_{2\text{D}}$, are quite similar, as evident from the comparison of Figs. 1(c) and 1(d). Note, however, that the SS and TB configurations are characterized by a different number of heterointerfaces, and then their comparative investigation

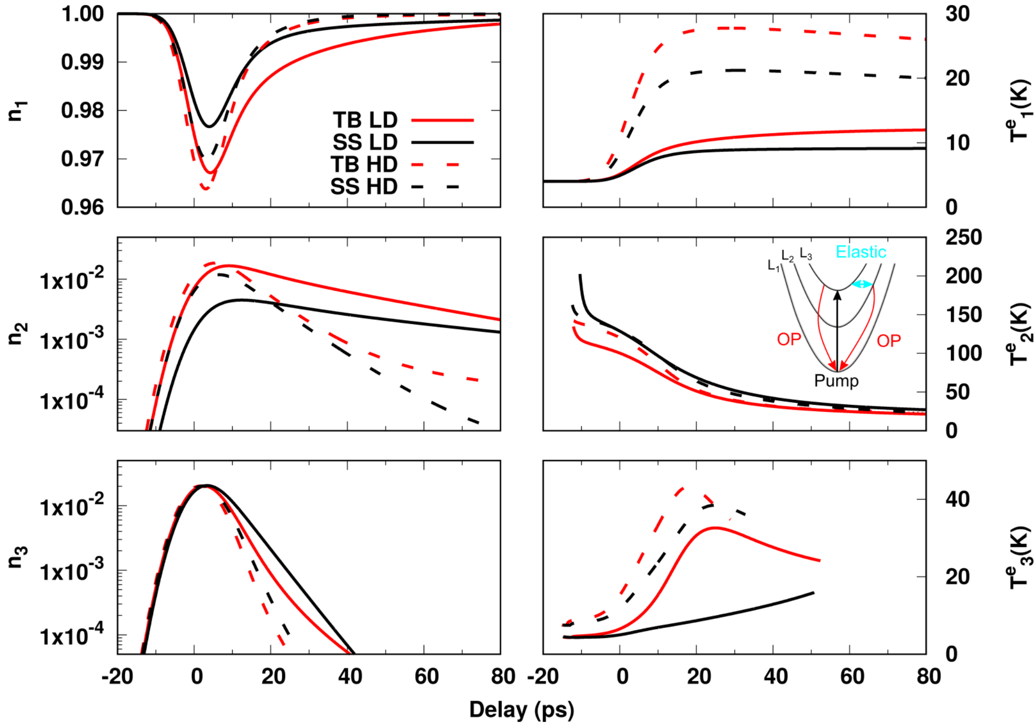

FIG. 2. (Left column) Population dynamics and (right column) electronic temperature for the fundamental and the first two excited states, at a lattice temperature $T^L = 4$ K, calculated for low-doping (LD) concentration ($n_{2D} = 5 \times 10^{10}$ cm^{-2}) and high-doping (HD) concentration ($n_{2D} = 5 \times 10^{11}$ cm^{-2}). For both the systems, the fluence of the pump was set to ensure a 2% peak population in L_3 ($n_3 = N_3/n_{2D} = 2\%$). In the inset, a schematics of the relaxation pathways discussed in the text is reported.

allows us to highlight the impact of IFR on carrier relaxation dynamics in n-type Ge/SiGe three-level systems.

We begin our discussion of the ISB relaxation dynamics by showing, in Fig. 2, the relative subband populations $n_i = N_i/n_{2D}$ and the associated electron temperatures T_i^e as a function of the delay time with respect to the pump beam, centered at $t = 0$ and chosen resonant with the $1 \rightarrow 3$ transition. The peak fluence $\tilde{I}(t = 0)$ associated to the pump pulse (see Appendix for the definition), and calculated in the AQCW region, has been tuned in the 0.87–1.44 kW/cm^2 range, to ensure a 2% peak in the relative population $n_3 = N_3/n_{2D}$ of the L_3 subband, a typical value achieved in pump-probe experiments [6,11,22]. For both the TB (red curves) and SS (black curves) configurations, results are reported for $T^L = 4$ K and two doping densities: $n_{2D} = 5 \times 10^{10}$ cm^{-2} (low doping, continuous curves) and $n_{2D} = 5 \times 10^{11}$ cm^{-2} (high doping, dashed curves). As expected, Fig. 2 shows that, upon increasing the doping density, the relaxation dynamics becomes faster due to the increased role of Coulomb scattering. Moreover, for the same n_{2D}, we find that in the SS system the relaxation rates are slower. This fact can be attributed to the diminished impact of the IFR scattering rate associated to the smaller number of heterointerfaces present in the SS configuration. Furthermore, the low value of the step in the SS potential profile suppresses the contribution to the scattering rate of this interface. As far as the subband electronic temperature is concerned, the model predicts modest excess values (<35 K) in L_1 and L_3, while T_2^e peaks around 150–200 K, at short delay times. To interpret these findings, we anticipate that elastic scattering channels play a dominant role in populating the L_2 subband.

In fact, in both the TB and SS configurations, the $3 \rightarrow 2$ transition assisted by phonon emission is forbidden. This is because, on the one end, the energy spacing E_{32}^0 is smaller than both the intravalley ($\hbar\omega_{\rm eff} = 37.07$ meV) and the intervalley ($\hbar\omega_{\rm eff} = 27.56$ meV) phonon energies [26] and, on the other end, this transition cannot be thermally activated, due to the relatively low-electron heating in level 3 induced by the pump (Fig. 2). It follows that the population of L_2 occurs via a two-step process $1 \xrightarrow{\text{pump}} 3 \xrightarrow{\text{elastic}} 2$ (see inset of Fig. 2), in line with the fact that the carrier density in the first excited subband peaks a few ps after the n_3 maximum. Elastic $3 \rightarrow 2$ events are responsible for the large excess temperature of L_2 since the potential energy in the initial state results in a large kinetic energy associated to the final level. Assuming instantaneous intrasubband thermalization times, these highly energetic carriers cause a significant increase in the electronic temperature of the L_2 subband. At this high T^e, the fraction of n_2 carriers with sufficient energy to relax into the L_1 subband via phonon emission is not negligible. Therefore, at small delay times, this mechanism represents a fast depopulation channel for L_2. At the same time, the phonon emission efficiently triggers a fast cooling of the subband since the OP emission rate assisting the $2 \rightarrow 1$ transition is larger for the L_2 carriers with higher energy. In turn, at larger delay times, the cooling quenches further emission of optical phonons, this resulting in increasingly slower depopulation rates. Therefore, a multiscale dynamics is observed for the n_2 carriers. To this regard, we note that a multiscale depopulation, controlled by pump-induced electron heating effects, has been

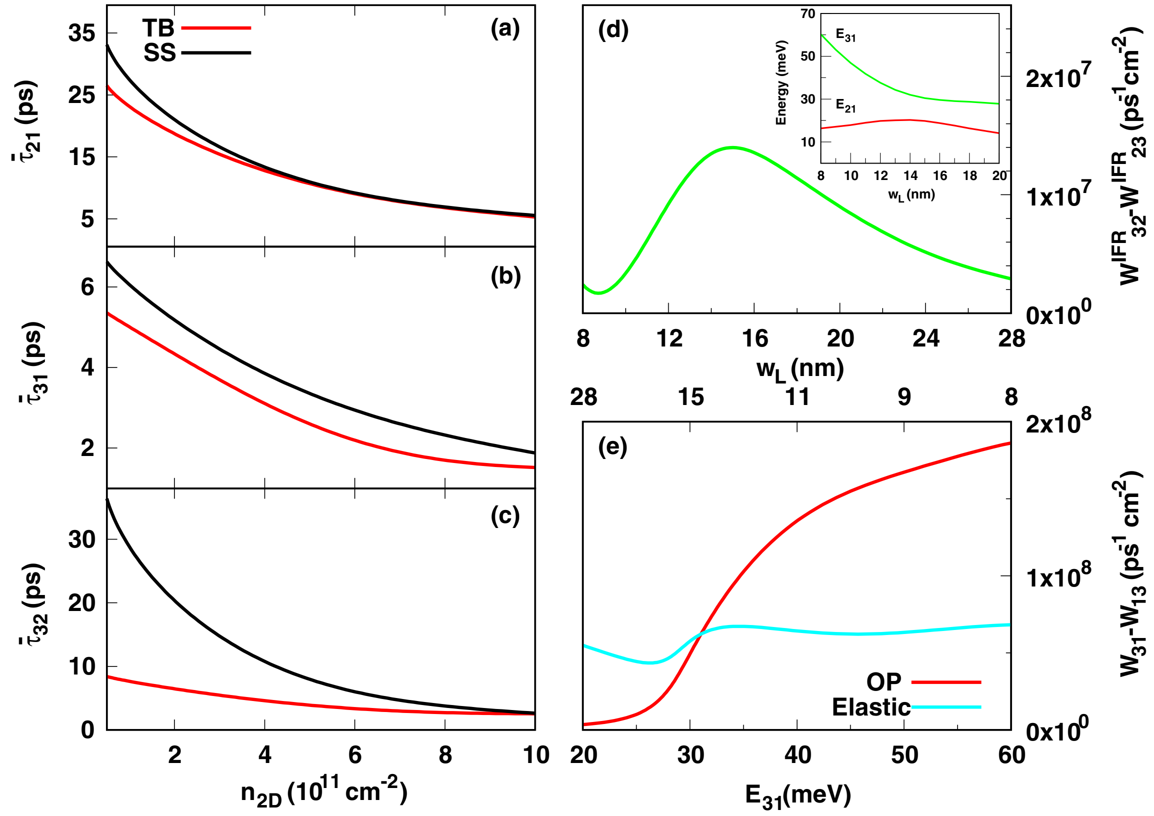

FIG. 3. (a)–(c) Relaxation times as a function of the doping concentration n_{2D} for the TB and SS systems (red and black curves, respectively). Since the population dynamics follows a nonsingle exponential behavior, the lifetimes have been averaged over the 0–50 ps delay range. For the highly doped TB configuration: (d) Net transition rate of the interface roughness channel as a function of the width w_L of the wide quantum well. In the inset, the corresponding E_{31} and E_{21} transition energies are reported as a function of w_L. (e) Net transition rate of the optical phonon channel and of the elastic channels as a function of the E_{31} transition energy (the corresponding w_L values are displayed in the top horizontal axis). The net transition rates reported in (d) and (e) are evaluated at the pump-pulse maximum. For all the panels, the lattice temperature is $T^L = 4$ K and the pump fluence is set to ensure a 2% peak population in L_3. Imposing $n_3 = 2\%$ required varying the pump fluence as follows: (a)–(c) 0.84–1.4 kW/cm^2, (d), (e) 2.6–620 kW/cm^2.

also observed for III-V [10] and SiGe-based [11] two-level MQW systems, when the subband energy is below the phonon threshold. A single exponential behavior is instead predicted for the depopulation of n_3. In fact, the n_3 dynamics is mainly controlled by energy-allowed $3 \rightarrow 1$ transitions mediated by optical phonon emission since $E^0_{31} > \hbar\omega_{\text{eff}}$. Additional minor contributions from elastic processes are present which have a more significant role in the high-doping regime, due to faster Coulomb scattering processes.

The framework proposed to interpret the results of Fig. 2 is supported by studying the intersubband relaxation times as a function of the n_{2D} equilibrium carrier density. To this end, we plot, in Figs. 3(a)–3(c), the $i \rightarrow j$ relaxation times, defined as $\bar{\tau}_{ij} = \langle \frac{n_i}{W_{ij}} \rangle$, where W_{ij} is the total transition rate. Due to its time-dependent character, the relaxation times were calculated averaging over the first 50 ps after the pump peak. The increasing Coulomb scattering rates associated to larger carrier densities are responsible for the monotonic decreasing behavior observed for all the $\bar{\tau}_{ij}$. In the large doping density regime, $\bar{\tau}_{ij}$ relaxation times in the TB and SS ACQWs show the same asymptotic value since, in this limit, the carrier relaxation dynamics is dominated by the Coulomb scattering which occurs at similar rate in the two configurations, due to the similarity of the wave functions and energy spacings. In the opposite limit of low doping density, the TB ACQW displays faster relaxation times, which are due to the larger contribution stemming from the IFR channel. In fact, in this system the tunneling barrier is associated to two heterointerfaces with large band offset, while the QW step in the SS sample is defined by a single heterointerface with a lower band offset. In line with this observation, we find that the larger difference between the relaxation times of the SS and TB systems is found for $\bar{\tau}_{32}$, being this transition mainly controlled by the IFR channel, as discussed later. We note that the dominance of the IFR scattering rate is a consequence of the specific system design, which is aimed at obtaining comparable $1 \rightarrow 2$ and $1 \rightarrow 3$ oscillator strengths. This condition is realized when the first- and second-excited wave functions are delocalized over the entire ACQW region. As a consequence, the wave-function amplitudes at the tunneling or step heterointerfaces are significantly different from zero and this, in turn, makes the contribution of the IFR scattering channel to the $3 \rightarrow 2$ transition rate to be particularly relevant. Such considerations are supported by the data reported in Fig. 3(d) where we show the net IFR intersubband rate $W^{\text{IFR}}_{32} - W^{\text{IFR}}_{23}$, as a function of the large well width w_L, calculated for the exemplificative case of the TB system at $n_{2D} = 5 \times 10^{11}$ cm^{-2}. We find a non-monotonic behavior with a maximum at about $w_L = 15$ nm,

i.e., quite close to the value of 13.0 nm adopted for the TB structure [see Fig. 1(a)]. For the same range of w_L, it is clear, from the inset of Fig. 3(d), that the difference between the E_{31} and E_{21} transition energies has a minimum, as expected around the anticrossing point. This suggests that the peak value of $W_{32}^{\mathrm{IFR}} - W_{23}^{\mathrm{IFR}}$ is indeed associated to the anticrossing condition. From a more general perspective, these observations also indicate that, in TB three-level systems, the strong hybridization of the first two excited states, which is typically required to efficiently pump the 1-3 transition, is unavoidably accompanied by large IFR scattering rates between L_2 and L_3.

Differently from what is observed for the $3 \rightarrow 2$ relaxation time, the $3 \rightarrow 1$ transition, for which we estimate the fastest scattering rates, is characterized by comparable values of $\overline{\tau}_{31}$ in the TB and SS configurations. In fact, given the large E_{31} transition energy, nonradiative relaxation rates are dominated by fast phonon-mediated intersubband scattering events which display comparable rates in the SS and TB configurations due to the similarity of the wave functions. To better evidence this point, in Fig. 3(e) we show, for the TB configuration, the $W_{31}^{\mathrm{OP}} - W_{13}^{\mathrm{OP}}$ net scattering rate (red curve), calculated at the pump-pulse maximum ($t = 0$) as a function of E_{31} (bottom axis) and w_L (top axis). This highlights the dependence of the OP scattering rate between levels 3 and 1 on the subband energy separation. As for comparison, the cyan curve in Fig. 3(e) represents the corresponding net scattering rate associated to all the other (elastic) scattering channels. As expected, we observe a kink in the red curve at an energy separation E_{31} of $\approx$27 meV, i.e., at the lowest phonon energy used to describe electron-phonon interaction. Indeed, the shape of the red curve is somehow reminiscent of a steplike function, which typically describes the deformation potential interaction in nonpolar materials where the electron-phonon coupling is invariant with respect to the exchanged momentum. By comparing the elastic and inelastic contributions to the total net rate $W_{31} - W_{13}$, it is clear that the elastic scattering channels are dominant only when $E_{31} \lesssim 27$ meV. Above the phonon threshold, instead, the OP contribution prevails.

Before continuing our channel-resolved analysis, it is useful to attempt a comparison between the relaxation time data in Figs. 3(a)–3(c) and experimental values reported in the literature. We remark, however, that this comparison is not straightforward since the relaxation dynamics in a pump-probe experiment is affected by setup specific conditions, such as the efficiency of the optical coupling between the pump beam and the sample, which hinder a precise estimation of the pump beam intensity in the MQW region. Similarly, the detuning of the pump photon energy with respect to the intersubband resonance may greatly affect the electron temperature and, as a result, the relaxation dynamics. In addition, the specific sample quality, in terms of lattice defects and interface roughness parameters, also severely impacts the observed relaxation times. Finally, most literature data have been obtained by pumping the first-excited level in two-level Si-rich MQW structures. For instance, in Ref. [33], Heiss *et al.* reported a τ_{21} relaxation time of ~30 ps by pumping the $1 \rightarrow 2$ transition at about 35 meV in an *n*-type Si-rich Si/SiGe QW system, featuring a $n_{2\mathrm{D}}$ carrier density of 10^{12} cm^{-2}. Such long relaxation time can be explained considering that, in Si-rich systems, the phonon threshold is at about 60 meV and, thus, well above the resonance energy. As a matter of fact, similarly large values have been also obtained in *p*-type Si-rich SiGe/Si QWs, resonantly pumped at about 30 meV [34,35]. Relatively long (10-ps) relaxation times, approximately constant in the 4–100 K lattice temperature range, have been observed in another set of *p*-type Si-rich SiGe/Si QWs, pumped well below the phonon energy [36]. Since in these systems the holes are confined in the SiGe layer, the authors concluded that the relaxation timescale is dominated by the (elastic) alloy scattering mechanism which instead, in the *n*-type Ge/SiGe system, is expected to play a negligible role [19]. Conversely, in *p*-type SiGe structures, when the resonance energy is well above the phonon threshold, e.g., by pumping the HH1 → HH2 at ~160 meV, subpicosecond relaxation times have been reported [37]. We note that such shortening of the relaxation time below the ps scale for transitions above the phonon energy has been also observed in pump-probe experiments performed with III-V based multilayer system [38–40]. Focusing instead on *n*-type Ge-rich structures, by pumping two-level MQW systems below the phonon energy, long relaxation times of tens of picoseconds, and roughly independent of temperature up to ~100 K, have been measured [22]. Well matching these experimental observations, our model suggests that subband energy spacings below the OP energy are associated to ISB particle fluxes occurring at a temporal scale in the order of tens of ps, mainly controlled by elastic channels. On the other hand, when the energy separation approaches the OP threshold, we predict a drastic increase of the relaxation rates dominated by the OP emission channel, driving the temporal scale well below the 10-ps scale, in agreement with Ref. [37]. Nevertheless, the relaxation times estimated by our model remain longer than the typical subpicosecond values obtained for III-V based materials with comparable energy spacing, due to the weaker electron-phonon coupling induced by the deformation potential in the *n*-type Ge/SiGe system [11]. On the other end, we find comparable relaxation times as in III-V structures, for all the regimes where the OP channel plays a minor role [10,41], provided that the interface quality of the group-IV based systems is sufficiently high, as for instance in Ref. [15].

To gain a deeper insight into the interplay between elastic and inelastic channels, we have performed a time- and channel-resolved analysis of the intersubband transition rates. To this aim, for each couple of levels (i, j), we plot, in Fig. 4, the net transition rate $W_{ij} - W_{ji}$ associated to each scattering channel as a function of the delay time. Data have been calculated for the TB (left panels) and SS (right panel) geometries, both at the high-doping (upper panels) and low-doping (lower panels) concentration. In keeping with previous observations, at the same doping density, the IFR scattering rate (green curve) for the SS system is lower than that obtained for the TB one, while comparable values are obtained for the other scattering channels. For delay times > 20 ps, at low-doping concentration the largest $3 \longleftrightarrow 1$ and $2 \longleftrightarrow 1$ intersubband rates in the TB system are associated to the IFR scattering, while, in the SS case, the dynamics is dominated by the Coulomb interaction (blue curve). Upon increasing the doping concentration, also in the TB system, the $3 \longleftrightarrow 1$ and

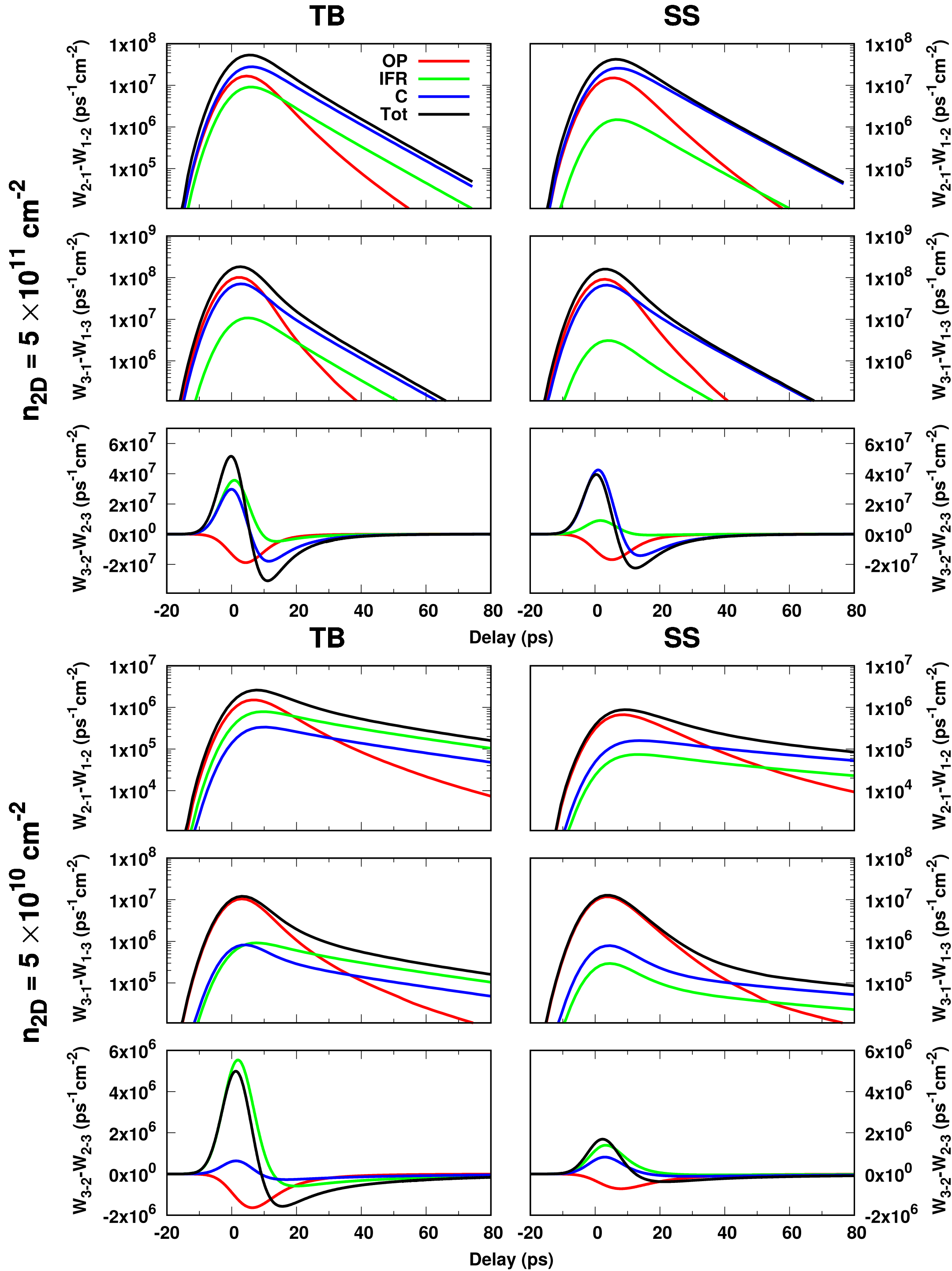

FIG. 4. Net transition rates between subbands i and j as a function of delay time with respect to the pump pulse centered at $t = 0$, resolved by scattering channel at $T^L = 4$ K. Top and bottom panels refer to the high- and low-doping concentration, respectively. Data referring to the TB (SS) structure are reported in the left (right) column. The color code identifying each scattering channel is the following: optical phonon (red), interface roughness (green), Coulomb (blue), total rate (black). The fluence of the pump was set to ensure a 2% peak population in L_3 and varies in the 0.87–1.44 kW/cm^2 range.

$2 \longleftrightarrow 1$ scattering rates are mainly driven by the Coulomb channel.

At short delay times, we observe that, both for the high- and low-doping regimes, the electron-OP interaction makes the largest contribution to the total $3 \longleftrightarrow 1$ and $2 \longleftrightarrow 1$ scattering rates, except for the case of $W_{21} - W_{12}$ in the high-doping condition, where the largest rates are still associated to the Coulomb interaction. The OP channel is dominant because the $3 \rightarrow 1$ intervalley OP relaxation mediated by phonon emission is activated by design ($E_{31} > 27.56$ meV). On the other end, the high electron temperature of the L_2 subband at this early stage of the relaxation dynamics (see right

central panel in Fig. 2) thermally activates fast intervalley phonon-assisted $2 \rightarrow 1$ transitions. These transitions become suppressed at later delay times when T_2^e cools down because of the small E_{21} separation.

While in the $3 \longleftrightarrow 1$ and $2 \longleftrightarrow 1$ net transition rates discussed insofar, back scattering events (i.e., from a lower-energy to a higher-energy subband) play a negligible role, this is not the case for the particle flux between levels 3 and 2, as evident from the sign reversal of the corresponding total net transition rate occurring around 10 ps, predicted for the TB and the SS structures both at high- and low-doping concentrations (see bottom panels of Fig. 4). In particular, the OP channel (red curve) gives a negative contribution to the net rate also for delay times <10 ps, i.e., when the pump beam is not extinguished. Such behavior can be explained considering the initial high electron temperature of L_2 caused by the $3 \rightarrow 2$ elastic scattering of carriers. In fact, the L_2 electrons, elastically scattered from the L_3 subband, feature high kinetic energy, as already discussed above. Since in our model instantaneous intrasubband thermalization is assumed, a non-negligible fraction of L_2 electrons is redistributed over an energy range which includes much larger values than those associated to the initial states of the $L_3 \rightarrow L_2$ elastic transition. These highly energetic L_2 electrons have sufficient energy to back scatter close to the E_3 subband minimum, emitting an OP (mainly in an intervalley process), while energy conservation suppresses the inverse $3 \rightarrow 2$ event because of the small energy spacing E_{32} and the relatively low electron temperature in the L_3 subband. Despite the negative contribution of the OP channel, the total $3 \longrightarrow 2$ net transition rate at the early stage of the dynamics remains larger than zero (delay <10 ps), being dominated by the contributions of the Coulomb and IFR channels which are positive, as a result of the population inversion realized between the L_3 and L_2 subbands. Conversely, at larger delay time, also those mechanisms induce back-scattering fluxes since the population of L_3 becomes much lower than that in L_2 one (see Fig. 2), due to the fast L_3 depopulation, mainly triggered by efficient $3 \rightarrow 1$ scattering processes.

This analysis demonstrates that the developed model allows us to address the impact of each scattering channel as well as its dependence on the design geometry adopted and doping regime. As a further step, since the investigated material system may be of interest to achieve CMOS-compatible laser devices in the THz range, we have also run a set of simulations targeting the investigation and optimization of the population inversion between L_3 and L_2, by varying the design parameters and the lattice temperature. As a matter of fact, in the so-called quantum fountain architecture, ACQW systems have been studied in the past to demonstrate three-level optically pumped coherent amplifiers where the upper and lower laser level is represented by the L_3 and L_2 subband, respectively [42–44]. We focus, as relevant physical quantity for optical amplification, on the time integral $\mathfrak{N}_{32} = \int_{\Delta t} [N_3(t) - N_2(t)]dt$ calculated in the time range where $N_3 > N_2$. Despite not having estimated the net material gain, due to the lack of experimental inputs for free-carrier absorption in n-type Ge/SiGe 2D structures, our data provide useful hints to restrict the design parameter space in view of subsequent studies. To this end, in Fig. 5, we calculate

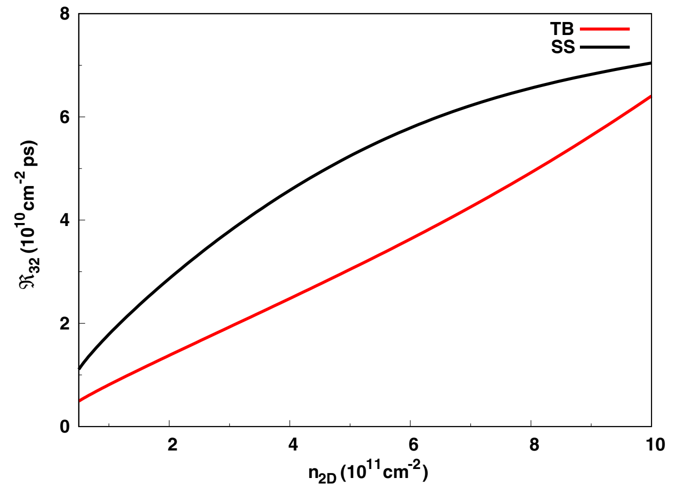

FIG. 5. Population difference between L_3 and L_2, integrated over the delay time in the t region where $N_3 > N_2$, as a function of n_{2D} at $T^L = 4$ K. The red and black curves refer to the TB and SS configurations, respectively. The pump fluence was monotonically increased in order to ensure a constant peak value of the relative population $n_3 = N_3/n_{2D}$.

$\mathfrak{N}_{32}$ as a function of n_{2D}, varying the pump-power density in order to keep the peak value of the n_3 relative population at 2%. Hence, the pump fluence in the quantum-well region was tuned in the 1.4–2.7 kW/cm^{-2} interval, for n_{2D} spanning the $1–10 \times 10^{11}$ cm^{-2} range. Both the curves referring to the TB and SS systems show a monotonic increasing behavior, but larger inversion values are predicted for the latter, due to the longer relaxation times resulting from the reduction of the IFR scattering rate in the SS structure. Since we expect that free-carrier absorption is mainly due to the interaction of photons with the electrons of the fundamental subband, which features very similar envelope functions for the two systems, optical losses in the TB and SS designs are expected to be approximately equal. This makes the SS architecture more suitable to achieve optical amplification in the explored doping range. Hence, we selected the SS configuration to further optimize $\mathfrak{N}_{32}$ as a function of the two geometrical parameters w_L and w_S.

For such configuration, we report in Fig. 6 the time-integrated population difference displayed as a function of w_L (black curve) by keeping the w_S thickness fixed at the same value as in Fig. 1(b) (15 nm) and setting $n_{2D} = 5 \times 10^{11}$ cm^{-2}. The fluence of the pump was set to $I = 1.3$ kW/cm^2, and its wavelength tuned to resonance at the $1 \rightarrow 3$ transition energy which varies upon changing w_L. The curve peaks at $w_L \approx 9.2$ nm, corresponding to an energy separation E_{32} of $\approx$17 meV. By looking at the oscillator strength f_{13} in the same w_L range (blue curve), it is clear that the driving force which controls the functional dependence of the population inversion is the pumping efficiency. The nonmonotonic behavior of f_{13} with w_L is, in turn, controlled by the variation of the overlap between the L_1 and L_3 envelope wave functions, a quantity that peaks around 9 nm (not shown). After fixing w_L at this optimal value, we varied the thickness w_S of the $Si_{0.03}Ge_{0.97}$ step, again maintaining the pump energy resonant with the $1 \rightarrow 3$ transition. As shown in

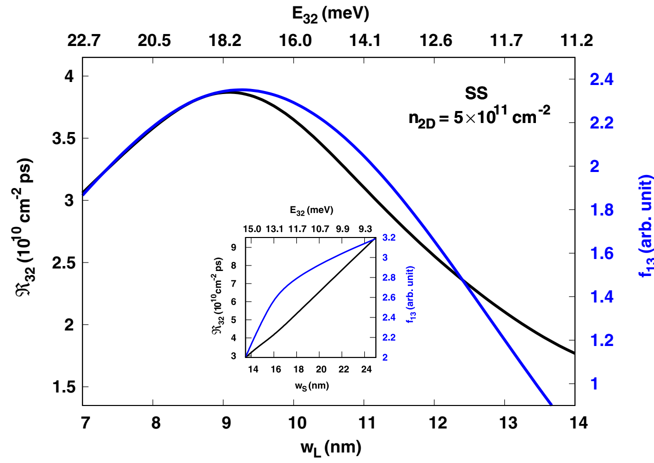

FIG. 6. (Black curve) Time-integrated population difference $N_3 - N_2$ and (blue curve) f_{13} oscillator strength as a function of the well width w_L for the SS configuration with $n_{2D} = 5 \times 10^{11}$ and a step thickness $w_S = 14.5$ nm at $T^L = 4$ K. The corresponding E_{32} energy is reported in the upper horizontal axis. In the inset the same quantity is plotted as a function of w_S for $w_L = 9.2$ nm. The pump fluence was fixed at 1.3 kW/cm^2.

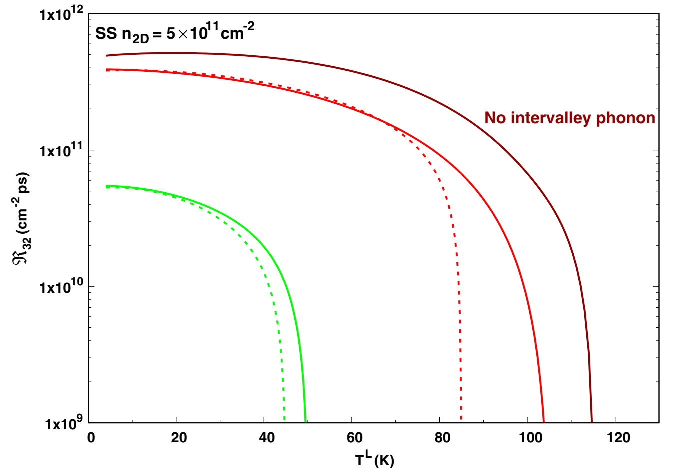

FIG. 7. Time-integrated population difference $N_3 - N_2$ as a function of the lattice temperature T^L at $n_{2D} = 5 \times 10^{11}$ for the SS configuration with $w_L = 9$ nm. 2% and 15% peak excitation values are represented by the green and red curves, respectively. The solid (dashed) curve corresponds to $w_S = 15$ ($w_S = 25$) nm. The intervalley optical phonon has been switched off in the dark red curve ($w_S = 15$ nm and 15% peak excitation degree).

the inset of Fig. 6 (black curve), the obtained $\mathfrak{N}_{32}$ data display an increasing monotonic behavior, which, again, follows the rising of the f_{13} oscillator strength (blue curve) with w_S. Note, however, that while the slope of f_{13} diminishes in the large w_S range, no slope change is observed in the data referring to the time-integrated population inversion (black curve). This is likely due to the fact that, upon increasing w_S, the E_{13} energy separation is lowered from 35.7 to 24.9 meV (i.e., below the lowest phonon energy), thus reducing the detrimental OP contribution to the total $3 \rightarrow 1$ relaxation rate. However, since E_{32} decreases with w_S, we remark that, when pumping the $1 \rightarrow 3$ transition in a design featuring E_{32} smaller than the pump spectral width, the $1 \rightarrow 2$ transition would be also excited. To avoid it, for a half-width at half-maximum (HWHM) of the pump of 5 meV, as in our case (see Appendix), w_S should not be larger than approximately ≈25 nm.

Since group-IV materials represent a promising platform to increase the maximum operating temperature in intersubband THz optical emitters, thanks to their weaker electron-phonon interaction, we conclude this section discussing the temperature behavior of the population inversion between L_3 and L_2. To this aim, in Fig. 7, we show $\mathfrak{N}_{32}$ as a function of the lattice temperature T^L, at $w_L = 9$ nm and $n_{2D} = 5 \times 10^{11}$, for two different values of w_S, i.e., $w_S = 15$ nm (solid curves) and $w_S = 25$ nm (dashed curves). To obtain these data, the pump pulse has been continuously tuned to keep it resonant with the $1 \rightarrow 3$ transition, so as to guarantee a 2% (green curves) or 15% (red curves) peak population in the L_3 subband. This required to vary the pump fluence between a minimum value of 0.4 kW/cm^2, adopted for the $w_S = 25$ nm system at low temperature, to the maximum value of 16.5 kW/cm^2, used for the $w_S = 15$ nm geometry at $T^L = 80$ K. Data in Fig. 7 highlight features of the intersubband relaxation dynamics related to the lattice temperature, evidencing the effect of a different excitation value as well as that of varying the subband energy spacing. As a matter of fact, for $w_S = 15$ nm, we obtain $E_{13} = 33.3$ meV, while, at $w_S = 25$ nm, E_{13} is reduced to 25.0 meV, i.e., below the intervalley OP energy. In the low pumping regime (green curves), the two geometries investigated show a very similar behavior, as expected from sharing comparable values for the low-temperature degree of population inversion and for the critical temperature at which the population inversion is lost ($40 < T^L < 50$ K). This fact indicates that the suppression of the $3 \rightarrow 1$ relaxation via OP emission, occurring in the $w_S = 25$ nm system, is not effective in increasing the critical temperature. Its beneficial effect is limited to a reduction of a factor ≈3 in the pump fluence required to achieve the 2% excitation level, with respect to the one used for the $w_S = 15$ nm system, as a result of the slower OP emission rate and of the larger f_{13} oscillator strength obtained for $w_S = 25$ nm. The absence of any increase in the critical temperature is due to the fact that, for lattice temperatures $T^L \simeq 45$ K, the thermal equilibrium population of L_2 becomes not negligible, being, for both the configurations, in the order of ≃ 1.2%–1.8%, thus comparable to the 2% excitation level in L_3. The impact of this detrimental effect is larger in the $w_S = 25$ nm system where the subband energy spacing is smaller. In this case, in fact, $E_{12} = 17.4$ meV, which is to be compared with a value of 19.3 meV estimated for the $w_S = 15$ nm geometry. As a consequence, the equilibrium thermal population of L_2 in the $w_S = 25$ nm geometry is higher, resulting in a lower critical temperature. By increasing the excitation to 15% (red curves), larger $\mathfrak{N}_{32}$ values are obtained. Again, at low T^L, the two systems share the same degree of population inversion and, also in this case, a lower critical temperature (≈ 80 K) is predicted for the $w_S = 25$ nm geometry (dashed curve) with respect to the $w_S = 15$ nm one (solid curve), where $\mathfrak{N}_{32}$ quenches at $T^L \approx 100$ K. The values obtained for the critical temperature and, in particular, the faster quench of $\mathfrak{N}_{32}$ for

the $w_S = 25$ nm structure, can be again attributed to the role played by the equilibrium thermal population of the L_2 level.

Finally, it has been proposed in literature that the coupling of electrons to large-momentum OPs mediating intervalley transitions might be suppressed in multilayer n-type Ge/SiGe heterostructures [9,11]. To assess the impact of this hypothesis on our predictions, we artificially turned off such relaxation pathway in the simulations for $w_S = 15$ nm, obtaining the dark red curve in Fig. 7. It can be clearly observed that, despite an overall increase in the population inversion $\mathfrak{N}_{32}$, the critical temperature is only marginally enhanced. Therefore, also in this favorable case, the implementation of a three-level quantum fountain architecture in the n-type Ge/SiGe ACQW system is not very promising to achieve optical amplification close to room temperature. In fact, from the above considerations, it emerges that the equilibrium thermal population of L_2 represents the main limiting factor which cannot be overcome by increasing the E_{21} energy separation because of the design restraints associated to the relatively small band offset in this material system ($\approx$120 meV). Recent calculations performed with n-type Ge/SiGe cascade structures indicate that the larger design degree of freedom offered by QCL architectures, where excitation and population inversion are driven by electric field, provides a doable path to reach room-temperature lasing operation.

IV. CONCLUSIONS

We developed a rate-equation model which includes both inelastic and elastic carrier scattering mechanisms to describe the ISB carrier relaxation dynamics occurring after pulsed optical excitation in n-type Ge/SiGe heterostructures. Moreover, by tracking the ISB particle and energy fluxes, under the assumption that intrasubband thermalization is achieved at a subpicosecond timescale, we were able to estimate the time-dependent electron temperature in each subband level. By applying the developed model to the case of the resonant pumping of the $L_1 \rightarrow L_3$ transition in three-level Ge/SiGe ACQWs systems, we were able to disentangle the time-dependent relative contributions to the ISB relaxation rate due to the emission of optical phonons, and the scattering due to interface roughness, ionized-impurity, and electron-electron interaction. A comparative analysis of different ACQW geometries and design parameters evidenced the critical role played by back-scattering events and electron heating effects on the relaxation dynamics, due to the very efficient L_3-L_1 elastic scattering. Our estimation of the time-dependent ISB relaxation times indicates lower rates with respect to comparable systems based on III-V materials. This has been attributed to the weaker electron-phonon coupling featured by nonpolar lattices. On the other end, the predicted relaxation rates are in line with experimental results reported for p-type and n-type SiGe multilayer samples at comparable ISB energy spacing. Finally, motivated by recent theoretical predictions suggesting room-temperature operation of n-type QCL structures based on Ge/SiGe MQW stacks, we explored the configuration parameter space for optimizing the population inversion between L_3 and L_2. As a following step, we studied this optimized system as a function of the lattice temperature, and found that population inversion drops rapidly when T^L approaches 120 K, mainly due to the thermal excitation in L_2 of a significant fraction of the carrier density, driven by the small energy separation with level L_1. This result severely questions the possibility to achieve a quantum fountain device able to operate at room temperature and based on this kind of simple three-level systems. As a consequence, despite the more demanding growth design and fabrication requirements, the electrically pumped quantum cascade architecture should be regarded as the most promising strategy for light emission in the THz range at room temperature, leveraging on Si-compatible heterostructures. In this perspective, we plan to calibrate, against experimental pump-probe data, the values adopted for the material parameters which control some of the scattering mechanisms (mainly the IFR and the electron-phonon scattering). These refined values will then subsequently be used to feed numerical simulation aimed at assessing the performance of n-type Ge/SiGe QCL devices.

ACKNOWLEDGMENTS

This work is supported by the European Union research and innovation program Horizon 2020 under Grant No. 766719 FLASH Project.

APPENDIX: DESCRIPTION OF OPTICAL PUMPING AND SCATTERING CHANNELS

1. Optical pumping

The particle rate induced by the quasimonochromatic pump pulse ($W^{\text{pump}}_{i\rightarrow j}$), featuring a pump fluence inside the ACQW region $\tilde{I}(t)$, a propagation angle with respect to the growth direction θ, and a polarization vector $\hat{\mathbf{e}}$, is expressed in terms of the optical cross section σ through the following set of equations:

$$W^{\text{pump}}_{i\rightarrow j}(E_i) = \frac{\sigma \tilde{I}}{\hbar\omega_p \cos\theta}, \tag{A1}$$

$$\sigma = \frac{e^2\pi\hbar}{2\epsilon_0 cnm_0}\left[\frac{(\Gamma/\pi)2E^0_{ji}2\hbar\omega_p}{\left[\left(E^0_{ji}\right)^2 - (\hbar\omega_p)^2 + \Gamma^2\right]^2 + (2\hbar\omega_p\Gamma)^2}\right] \times \frac{\sum_{\gamma=1}^4 f^\gamma_{ij}}{4}, \tag{A2}$$

$$f^\gamma_{ij} = \frac{2m_0}{E^0_{ji}}\left(\hat{e}_x w^\gamma_{xz} + \hat{e}_y w^\gamma_{yz} + \hat{e}_z w^\gamma_{zz}\right)^2 \left|p^z_{ij}\right|^2, \tag{A3}$$

where the $\hat{z}$ direction has been chosen parallel to the growth axis. In Eq. (A3), the γ index runs over the four degenerate L valleys and f^γ_{ij} is the associated $i \rightarrow j$ oscillator strength; p^z_{ij} is the dipole matrix element projected along z and w^γ_{mn} are the components of the inverse mass tensor for the γ valley. Level broadening has been phenomenologically introduced using a Lorentzian shape to describe the cross section as a function of the photon energy detuning with respect to the resonance energy $E^0_{ji} = E^0_j - E^0_i$. In the simulations, we set $\Gamma = 5$ meV, as suggested by recent ISB absorption data acquired from ACQW n-type Ge/SiGe samples [14]. Note also that, in Eq. (A2), effects related to the depolarization shift were neglected since they are not expected to significantly impact on the ISB dynamics. Consequently, the absorption

resonance energy was set equal to the bare ISB transition energy. The temporal profile of the beam intensity $\tilde{I}(t)$ in the ACQW region is modeled using a Gaussian profile centered at $t = 0$, whose duration (HWHM equal to 5 ps) is chosen to reproduce the bandwidth-limited Gaussian pulses typically produced at free-electron laser facilities [11,22].

2. Electron-phonon scattering

Inelastic interactions of 2D electronic carriers with the lattice excitations are modeled considering 3D bulklike phonons. To describe intervalley and intravalley scattering, we assume two effective dispersionless optical branches, characterized by different values of the phonon energy $\hbar\omega_{\mathrm{eff}}$ and of the deformation potential Ξ_{OP} (see Table I). In nonpolar crystals, the probability per unit of time for an electron in subband i to be scattered in subband j does not depend on the modulus of the exchanged momentum. Therefore, the rate is also independent of the initial electron energy. Its value is given by

$$W_{i\to j}^{\mathrm{OP}\mp}(E_i) = \frac{n_{\mathrm{dest}} m_d \,\Xi_{\mathrm{OP}}^2}{2\hbar^2 \rho\omega_{\mathrm{eff}}}\left[N(\omega_{\mathrm{eff}}, T^L) + \frac{1}{2} \mp \frac{1}{2}\right] F_{ij}. \quad (A4)$$

In Eq. (A4), $N(\omega_{\mathrm{eff}}, T^L)$ is the equilibrium Bose distribution at the lattice temperature T^L for phonons with energy $\hbar\omega_{\mathrm{eff}}$ and $F_{ij} = \int dz\, \psi_j^2(z)\psi_i^2(z)$, with $\psi_i(z)$ and $\psi_j(z)$ being the envelope functions in the ith and jth subband, respectively. n_{dest} is the number of degenerate L valleys which are involved in inter ($n_{\mathrm{dest}} = 3$) and intravalley ($n_{\mathrm{dest}} = 1$) processes.

The interaction with the acoustic branch cannot cause intersubband transitions, due to the small value of the phonon momentum. Nevertheless, the acoustic phonons induce in each subband an energy flux which is described in terms of the difference between T_i^e and T^L, following Ref. [45]. It is worth noting that, although included in our model, this effect is not significant at the temporal scale investigated [29].

3. Interface roughness scattering

The impact of nonideal heterointerfaces on the carrier dynamics is evaluated according to Ref. [46] where the scattering rate induced by the perturbing potential associated to the presence of IFR has been first calculated. Assuming a Gaussian distribution for the interface terrace height with a root mean square Δ and a terrace correlation length Λ, the IFR scattering rate for an electron in subband i with initial momentum $\mathbf{k}_i$ to subband j is given by

$$W_{ij}^{\mathrm{IFR}}(k_i) = \sum_I \frac{|F_{ij,I}\Delta\Lambda|^2 m_d}{\hbar^3}\int_0^{\pi} d\theta\, e^{-q^2\Lambda^2/4}, \quad (A5)$$

$$F_{ij,I} = \int_{z_I^-}^{z_I^+} dz\, \psi_j^*(z)\frac{dV(z)}{dz}\psi_i(z), \quad (A6)$$

where the index I runs over all the (decoupled) interfaces present in the multilayer stack, and the integral in Eq. (A6) is calculated in a neighborhood of the interface position z_I. The angular integral in Eq. (A5) is associated to the sum over all the available $\mathbf{k}_j$ states in the final subband j and q is the modulus of the exchanged momentum $\mathbf{q} = \mathbf{k}_j - \mathbf{k}_i$, which can be expressed as a function of k_i and of the scattering angle θ, exploiting the following relations:

$$k_i = \sqrt{\frac{2m_d\left(E_i - E_i^0\right)}{\hbar^2}},$$

$$k_j = \sqrt{k_i^2 - \frac{2m_d}{\hbar^2}E_{ji}^0}.$$

As for the interface roughness parameters, the values of Δ and Λ adopted in our simulation (see Table I) have been chosen relying on very accurate experimental results, recently obtained from ACQW Ge/SiGe heterostructures as described in Ref. [15].

4. Coulomb scattering

The presence of positively charged ions and other electrons also has a direct effect on the dynamics, giving rise to elastic scatterings by a Coulomb potential which depends on the density of positive ions and other electrons along the growth direction z. For the case of impurities, i.e., fixed ions infinitely heavy with respect to the electrons, this is given by the static concentration of dopants $n_{3\mathrm{D}}(z_0)$ [46,47], tailored to reproduce the typical spatial profile and broadening of donor concentration obtained from experiments. For the case of electrons, instead, a mean field approach is adopted to limit computational workload [48], i.e., the e-e interaction, which is a two-body process, is thus reduced to a single-particle scattering event. Each electron in a subband i is elastically scattered to the final subband $j \neq i$, interacting with the electron density $[|\psi_k(z_0)|^2]$ of subband $k = 1, 2, 3$ at each point in the growth direction. We thus consider a generalized expression for the scattering rates due to Coulomb interactions, where the II and the e-e contributions are distinguishable through their form factors

$$W_{ij}^{C}(k_i) = \frac{m_d e^4}{4\pi\hbar^3\epsilon^2}\int_0^{\pi} d\theta \frac{J_{ij}^{\mathrm{II}}(q_\alpha) + \sum_k J_{ij,k}^{\mathrm{ee}}(q_\alpha)}{(q_\alpha + q_{\mathrm{TF}})^2}, \quad (A7)$$

$$J_{ij}^{\mathrm{II}}(q_\alpha) = \int n_{3\mathrm{D}}(z_0)\left(\int dz\, \psi_j^*(z)e^{-q_\alpha|z-z_0|}\psi_i(z)\right)^2 dz_0, \quad (A8)$$

$$J_{ij,k}^{\mathrm{ee}}(q_\alpha) = \int n_k|\psi_k(z_0)|^2\left(\int dz\, \psi_j^*(z)e^{-q_\alpha|z-z_0|}\psi_i(z)\right)^2 dz_0. \quad (A9)$$

Finally, a Thomas-Fermi screening is applied through the wave vector $q_{\mathrm{TF}} = \frac{m_d e^2}{2\pi\hbar^2\epsilon}$.

[1] R. Köhler, A. Tredicucci, F. Beltram, H. E. Beere, E. H. Linfield, A. G. Davies, D. A. Ritchie, R. C. Iotti, and F. Rossi, Nature (London) **417**, 156 (2002).

[2] B. S. Williams, Nat. Photonics **1**, 517 (2007).

[3] M. S. Vitiello, G. Scalari, B. Williams, and P. De Natale, Opt. Express **23**, 5167 (2015).

[4] F. H. Julien, J. Lourtioz, N. Herschkorn, D. Delacourt, J. P. Pocholle, M. Papuchon, R. Planel, and G. Le Roux, Appl. Phys. Lett. **53**, 116 (1988).

[5] O. Gauthier-Lafaye, F. H. Julien, S. Cabaret, J.-M. Lourtioz, G. Strasser, E. Gornik, M. Helm, and P. Bois, Appl. Phys. Lett. **74**, 1537 (1999).

[6] D. Sabbagh, J. Schmidt, S. Winnerl, M. Helm, L. Di Gaspare, M. De Seta, M. Virgilio, and M. Ortolani, ACS Photonics **3**, 403 (2016).

[7] H. Schneider and H. C. Liu, *Quantum Well Infrared Photodetectors*, Vol. 126 (Springer, Berlin, 2007).

[8] D. Paul, Laser Photonics Rev. **4**, 610 (2010).

[9] G. Sun, H. H. Cheng, J. Menéndez, J. B. Khurgin, and R. A. Soref, Appl. Phys. Lett. **90**, 251105 (2007).

[10] B. N. Murdin, W. Heiss, C. J. G. M. Langerak, S.-C. Lee, I. Galbraith, G. Strasser, E. Gornik, M. Helm, and C. R. Pidgeon, Phys. Rev. B **55**, 5171 (1997).

[11] M. Virgilio, M. Ortolani, M. Teich, S. Winnerl, M. Helm, D. Sabbagh, G. Capellini, and M. De Seta, Phys. Rev. B **89**, 045311 (2014).

[12] M. De Seta, G. Capellini, Y. Busby, F. Evangelisti, M. Ortolani, M. Virgilio, G. Grosso, G. Pizzi, A. Nucara, and S. Lupi, Appl. Phys. Lett. **95**, 051918 (2009).

[13] T. Grange, D. Stark, G. Scalari, J. Faist, L. Persichetti, L. Di Gaspare, M. De Seta, M. Ortolani, D. J. Paul, G. Capellini, S. Birner, and M. Virgilio, Appl. Phys. Lett. **114**, 111102 (2019).

[14] C. Ciano, M. Virgilio, M. Montanari, L. Persichetti, L. Di Gaspare, M. Ortolani, L. Baldassarre, M. Zoellner, O. Skibitzki, G. Scalari, J. Faist, D. Paul, M. Scuderi, G. Nicotra, T. Grange, S. Birner, G. Capellini, and M. De Seta, Phys. Rev. Appl. **11**, 014003 (2019).

[15] T. Grange, S. Mukherjee, G. Capellini, M. Montanari, L. Persichetti, L. D. Gaspare, S. Birner, A. Attiaoui, O. Moutanabbir, M. Virgilio, and M. De Seta, Phys. Rev. Appl. **13**, 044062 (2020).

[16] L. Persichetti, M. Montanari, C. Ciano, L. Di Gaspare, M. Ortolani, L. Baldassarre, M. Zoellner, S. Mukherjee, O. Moutanabbir, G. Capellini, M. Virgilio, and M. De Seta, Crystals **10**, 179 (2020).

[17] M. De Seta, G. Capellini, M. Ortolani, M. Virgilio, G. Grosso, G. Nicotra, and P. Zaumseil, Nanotechnology **23**, 465708 (2012).

[18] Y. Busby, M. De Seta, G. Capellini, F. Evangelisti, M. Ortolani, M. Virgilio, G. Grosso, G. Pizzi, P. Calvani, S. Lupi, M. Nardone, G. Nicotra, and C. Spinella, Phys. Rev. B **82**, 205317 (2010).

[19] M. Virgilio, D. Sabbagh, M. Ortolani, L. Di Gaspare, G. Capellini, and M. De Seta, Phys. Rev. B **90**, 155420 (2014).

[20] C. Ciano, M. Virgilio, L. Bagolini, L. Baldassarre, A. Rossetti, A. Pashkin, M. Helm, M. Montanari, L. Persichetti, L. Di Gaspare, G. Capellini, D. J. Paul, G. Scalari, J. Faist, M. De Seta, and M. Ortolani, Photonics **7**, 2 (2019).

[21] C. Ciano, M. Virgilio, L. Bagolini, L. Baldassarre, A. Pashkin, M. Helm, M. Montanari, L. Persichetti, L. Di Gaspare, G. Capellini, D. J. Paul, G. Scalari, J. Faist, M. De Seta, and M. Ortolani, Opt. Express **28**, 7245 (2020).

[22] M. Ortolani, D. Stehr, M. Wagner, M. Helm, G. Pizzi, M. Virgilio, G. Grosso, G. Capellini, and M. De Seta, Appl. Phys. Lett. **99**, 201101 (2011).

[23] J. A. Levenson, G. Dolique, J. L. Oudar, and I. Abram, Phys. Rev. B **41**, 3688 (1990).

[24] A. Valavanis, Z. Ikonić, and R. W. Kelsall, Phys. Rev. B **77**, 075312 (2008).

[25] J. Wang, J.-P. Leburton, F. H. Julien, and A. Sa'ar, IEEE Photonics Technol. Lett. **8**, 1001 (1996).

[26] C. Jacoboni, F. Nava, C. Canali, and G. Ottaviani, Phys. Rev. B **24**, 1014 (1981).

[27] M. Montanari, M. Virgilio, C. L. Manganelli, P. Zaumseil, M. H. Zoellner, Y. Hou, M. A. Schubert, L. Persichetti, L. Di Gaspare, M. De Seta, E. Vitiello, E. Bonera, F. Pezzoli, and G. Capellini, Phys. Rev. B **98**, 195310 (2018).

[28] F. Hackl, M. Grydlik, P. Klenovský, F. Schäffler, T. Fromherz, and M. Brehm, Ann. Phys. **531**, 1800259 (2019).

[29] M. Virgilio, G. Grosso, G. Pizzi, M. De Seta, G. Capellini, and M. Ortolani, Phys. Rev. B **86**, 205317 (2012).

[30] K. Driscoll and R. Paiella, J. Appl. Phys. **102**, 093103 (2007).

[31] S. Lutgen, R. A. Kaindl, M. Woerner, T. Elsaesser, A. Hase, H. Künzel, M. Gulia, D. Meglio, and P. Lugli, Phys. Rev. Lett. **77**, 3657 (1996).

[32] F. Stern and W. E. Howard, Phys. Rev. **163**, 816 (1967).

[33] W. Heiss, E. Gornik, H. Hertle, B. Murdin, G. M. H. Knippels, C. J. G. M. Langerak, F. Schäffler, and C. R. Pidgeon, Appl. Phys. Lett. **66**, 3313 (1995).

[34] P. Rauter, T. Fromherz, N. Q. Vinh, B. N. Murdin, G. Mussler, D. Grützmacher, and G. Bauer, Phys. Rev. Lett. **102**, 147401 (2009).

[35] R. W. Kelsall, Z. Ikonic, P. Murzyn, C. R. Pidgeon, P. J. Phillips, D. Carder, P. Harrison, S. A. Lynch, P. Townsend, D. J. Paul, S. L. Liew, D. J. Norris, and A. G. Cullis, Phys. Rev. B **71**, 115326 (2005).

[36] P. Murzyn, C. R. Pidgeon, J.-P. R. Wells, I. V. Bradley, Z. Ikonic, R. W. Kelsall, P. Harrison, S. A. Lynch, D. J. Paul, D. D. Arnone, D. J. Robbins, D. Norris, and A. G. Cullis, Appl. Phys. Lett. **80**, 1456 (2002).

[37] P. Rauter, T. Fromherz, G. Bauer, N. Q. Vinh, B. N. Murdin, J. P. Phillips, C. R. Pidgeon, L. Diehl, G. Dehlinger, and D. Grützmacher, Appl. Phys. Lett. **89**, 211111 (2006).

[38] J. Faist, F. Capasso, C. Sirtori, D. L. Sivco, A. L. Hutchinson, S. N. G. Chu, and A. Y. Cho, Appl. Phys. Lett. **63**, 1354 (1993).

[39] R. Ferreira and G. Bastard, Phys. Rev. B **40**, 1074 (1989).

[40] P. Boucaud, F. H. Julien, R. Prazeres, J. Ortega, V. Berger, J. Nagle, and J. P. Leburton, Electron. Lett. **32**, 2357 (1996).

[41] B. N. Murdin, G. M. H. Knippels, A. F. G. van der Meer, C. R. Pidgeon, C. J. G. M. Langerak, M. Helm, W. Heiss, K. Unterrainer, E. Gornik, K. K. Geerinck, N. J. Hovenier, and W. T. Wenckebach, Semicond. Sci. Technol. **9**, 1554 (1994).

[42] J. B. Khurgin, G. Sun, L. R. Friedman, and R. A. Soref, J. Appl. Phys. **78**, 7398 (1995).

[43] J. Choe, A. G. U. Perera, M. H. Francombe, and D. D. Coon, Appl. Phys. Lett. **59**, 54 (1991).

[44] M. Helm, P. England, E. Colas, F. DeRosa, and S. J. Allen, Phys. Rev. Lett. **63**, 74 (1989).

[45] M. E. Daniels, B. K. Ridley, and M. Emeny, Solid State Electron. **32**, 1207 (1989).

[46] T. Ando, A. B. Fowler, and F. Stern, Rev. Mod. Phys. **54**, 437 (1982).

[47] P. Harrison and A. Valavanis, *Quantum Wells, Wires and Dots* (Wiley, Hoboken, NJ, 2016).

[48] T. Grange, Phys. Rev. B **89**, 165310 (2014).

[49] S. Gupta, D. Nam, J. Vuckovic, and K. Saraswat, Phys. Rev. B **97**, 155127 (2018).